https://doi.org/10.5194/wes-2025-275
Preprint. Discussion started: 16 January 2026

eawe european academy of wind energy
Open Access WIND ENERGY SCIENCE DISCUSSIONS

Optimal Control of Crosswind Kite Systems with an Engineering Wake Model based on Vortex Loops and Dipoles

Jochem De Schutter[1], Antonia Mühleck[1], Rachel Leuthold[1], and Moritz Diehl[1,2]

[1]Department of Microsystems Engineering, University of Freiburg, Georges-Köhler-Allee 102, 79108 Freiburg, Germany
[2]Department of Mathematics, University of Freiburg, Ernst-Zermelo-Straße 1, 79104 Freiburg, Germany

Correspondence: Jochem De Schutter (jochem.de.schutter@imtek.uni-freiburg.de) and Moritz Diehl (moritz.diehl@imtek.uni-freiburg.de)

Abstract. Modern crosswind kite systems provide a technological means to exert large aerodynamic forces in wind fields above the reach of conventional wind turbines, with applications in airborne wind energy (AWE) generation and wake regeneration above conventional wind farms. A central challenge in kite system optimization is to both accurately and efficiently model self-induction effects on system design, performance, and operation. Vortex-based models are a natural candidate for this task as they provide a wake resolution that allows to consistently capture kite-specific operating conditions. Existing vortex-based approaches have been developed under the assumption of static, axisymmetric flight, which is typically violated in practice. Therefore, we propose a vortex-based continuous-time wake model for simulation and optimal control of crosswind kites that is capable of capturing the unsteady, non-axisymmetric flight conditions induced by skewed inflow and gravity. The model represents the shed vorticity as a hybrid distribution of infinitesimal vortex-loops and dipole elements and shows good agreement with simulation results obtained with the free-vortex solver DUST, with the remaining discrepancies largely due to convection-velocity selection. As a second contribution, we introduce a transcription strategy to efficiently incorporate the new model into periodic optimal control problems (OCP), and examine the OCP solution sensitivity to transcription parameters in a numerical case study of a dual-kite system. Based on this sensitivity analysis, we find a transcription that solves the problem at three times the computational cost of the original OCP without wake model, while still retaining accuracy within $5\,\%$ compared to a highly resolved reference solution. The solution of the original no-wake problem deviates with $145\,\%$ compared to this reference solution. Overall, the framework enables the efficient and wake-aware optimal control of crosswind (multi-)kite systems and can be readily applied to industry-relevant applications such as single-kite airborne wind energy systems.

1 Introduction

Kite systems have a millennia-long history in human civilization, with significant roles in culture, science, and technology (Hart, 1982). In recent decades, advances in computing and materials science have reignited interest in these systems, motivating researchers and engineers to develop a new class of high-performance kite-based technologies. As envisaged by Loyd (1980), most of these technologies rely on soft or rigid tethered wings performing fast crosswind maneuvers to generate substantial aerodynamic forces, which can be harnessed for various applications such as ship towing (Fritz, 2013) or electricity generation through airborne wind energy (AWE) systems (Fagiano et al., 2022). A further, yet unrealized, concept is that of airborne atmospheric actuators, designed to redirect airflow from the atmospheric boundary layer surrounding wind farms to enhance their overall efficiency through wake recovery (Ploumakis and Bierbooms, 2018; Kokkedee, 2022; Van Niekerk, 2025).

One central engineering challenge for crosswind kite systems is the optimal co-design of the dynamic flight path of the kite together with its design parameters. Optimal control is a natural candidate tool for this task, due to its inherent ability to deal with nonlinear constrained systems with multiple in- and outputs, which has resulted to widespread use, mainly in research (Vermillion et al., 2021), but also in industry (Noga et al., 2024). Optimal control comes with the drawback of a high computational cost and implementation effort. However, after more than a decade of research on efficient formulations and solution strategies (Horn et al., 2013; Gros et al., 2013; Malz et al., 2020; Trevisi et al., 2022) as well as open-source software developments (De Schutter et al., 2023b), it is safe to say that efficient numerical optimal control of crosswind kite systems based on high-fidelity flight mechanics is readily available for control experts and non-experts alike.

In consequence, most current research in this field focuses on improving the fidelity of the optimization models, e.g., by incorporating more realistic and flexible tether representations (Heydarnia et al., 2025) or by improving upscaling models (Joshi et al., 2024). Another major modeling challenge concerns the self-induction of the kite system. Analogous to conventional wind turbines, the aerodynamic loading of crosswind kites generates a wake that is advected downstream. This wake, in turn, induces a local wind speed deficit at the kite position, thereby diminishing the available wind power. For horizontal-axis wind turbines, this self-blockage effect has been extensively studied and establishes a theoretical upper bound on the extractable wind power, widely known as the Betz limit (Manwell, J. F., McGowan, J. G. and Rogers, A. L., 2009).

Well-established induction modeling methods for horizontal-axis wind turbines are derived from momentum balance principles. However, these approaches cannot be directly applied to kite systems, as the fundamental assumptions that they rely on are typically violated. First, kite systems interact with the airflow over an annular rather than a full-disc region. Second, the aerodynamic loading is inherently non-uniform throughout a single crosswind loop. Third, the generated aerodynamic forces are often significantly misaligned with the freestream wind direction, a necessary condition to compensate for gravitational forces.

Therefore, in current engineering practice, self-induction effects are often neglected. Such a simplification is justified for existing small-scale prototypes, where relatively low aerodynamic loads act over large airborne areas. However, as system size and loading increase, and as flight trajectories are compacted to maximize power density, self-induction will become increasingly significant (Leuthold et al., 2017; Kheiri et al., 2019; Haas et al., 2019; De Schutter et al., 2023a). This effect is particularly pronounced in multi-kite configurations, where two or more wings fly tight crosswind loops around a shared main tether (Zanon et al., 2014). In conclusion, the accurate performance assessment of utility-scale kite systems requires the development of optimization-friendly engineering wake models capable of capturing self-induction effects.

Initial research efforts have primarily focused on extending momentum-based models to the kite system context by deriving analytical formulations under various simplifying assumptions: steady, axisymmetric flight (De Lellis et al., 2018; Kheiri et al., 2019; Kaufman-Martin et al., 2022); steady, non-axisymmetric flight (Akberali et al., 2021); and (unvalidated) unsteady, axisymmetric flight conditions (Zanon et al., 2014; Leuthold et al., 2018; De Schutter et al., 2018, 2023a). However, there is currently no validated momentum-based approach available that accurately accounts for all relevant kite operating conditions. Moreover, as noted by Gaunaa et al. (2020), when using the 3D polar of the kite wing, these generalizations are physically inconsistent, leading to a double-counting of the contribution of the wake directly trailing the wing. If one would alternatively resort to a momentum approach using the 2D polar of the kite, application-specific root and tip corrections would need to be developed.

To address this last issue of consistency, Gaunaa et al. (2020), and subsequently Trevisi et al. (2023), developed physically consistent self-induction models for the steady, axisymmetric case. Their approach employed vortex methods as outlined by Branlard (2017) and demonstrated good agreement with higher-fidelity free-vortex wake simulations. A more versatile but numerically more expensive approach is offered by adding a discrete lifting-line vortex model in the transcription process of a general, unsteady AWE optimal control problem (OCP) (Leuthold et al., 2024). In the aforementioned work, reasonable agreement of the vortex model with existing Large-Eddy Simulation results from the literature is reported. However, the computational cost of the OCP currently scales unfavorably with the number of vortex elements included, which might result in a prohibitive numerical expense in certain scenarios.

The contribution of this paper is the formulation of a new optimization-friendly self-induction wake model that is capable of capturing the inherently unsteady and non-axisymmetric operating conditions of kite systems. Rather than deriving a simplified analytical approximation or employing a discrete vortex model, we represent the coupled dynamics of the kite system and its wake continuously through a combined differential-algebraic equation (DAE) and partial differential equation (PDE) framework. The resulting continuous model is validated in relevant conditions against the higher fidelity free-vortex wake solver DUST. Finally, we demonstrate how the DAE–PDE-based OCP can be efficiently transcribed into a standard continuous-time OCP formulation and analyze the sensitivity of the resulting problem to key transcription parameters.

To limit the scope of this paper, we consider a kite system with fixed tether length, thereby excluding pumping-style AWE systems, which rely on tether reeling. However, the developed methods in this paper can be directly applied to these type of systems as well. We focus here on a dual-kite system model, to generate an interesting high-load scenario with significant induction effects. Similarly, application of the developed methods to single-kite systems is straightforward.

The remainder of this paper is organized as follows. Section 2 introduces the DAE model of a multi-kite system as described in the literature. Section 3 presents the vortex-based continuous wake model and its associated PDE dynamics. In Sect. 4, we present validation results by comparing model simulations with those from the free-vortex simulation framework DUST. Section 5 then formulates the coupled DAE–PDE OCP and discusses its efficient transcription into a continuous-time OCP form. Finally, Sect. 6 presents the results of a representative numerical case study.

2 Kite system model

In this section, we present the flight dynamics model of a dual-kite system, which is largely synthesized from the literature. As argued by Gros and Diehl (2013), for optimal control applications, it is beneficial to model the flight dynamics of tethered airfoils by an index-1 DAE such as:

$$F(x(t),\dot{x}(t),u(t),z(t),y(t,\cdot),\theta)=0\,, \quad \forall t\in\mathbb{R} \tag{1}$$

with states $x(t)$, controls $u(t)$, algebraic variables $z(t)$ and design parameters θ. We introduce here as a new element the wake representation $y(t,\tau)$. While the variable $t\in\mathbb{R}$ denotes the current physical time, the variable $\tau\in\mathbb{R}^+$ represents the age (or convection time) of a wake element, i.e. the time elapsed since that portion of the wake was generated at the boundary $\tau=0$. The evolution of the wake is described by the inhomogeneous transport equation:

$$\frac{\mathrm{d}y}{\mathrm{d}t}(t,\tau)+\frac{\mathrm{d}y}{\mathrm{d}\tau}(t,\tau)=f(y(t-\tau,\cdot))\,, \quad \forall(t,\tau)\in\mathbb{R}^2\,, \tag{2}$$

with the boundary condition

$$y(t,0)=g(x(t),y(t,\cdot))\,, \quad \forall t\in\mathbb{R}\,. \tag{3}$$

Thus, overall, the kite system dynamics are described by a coupled DAE-PDE system. In this section, we focus solely on the DAE part of the dynamics. Section 3 then later describes in detail the wake parametrization $y(t,\tau)$ and the source term function f and boundary condition function g.

2.1 Dual-wing flight dynamics

While high-fidelity 6DOF aircraft models are available in the literature and open-source software, we limit ourselves here to the more simple point-mass model as proposed by Zanon et al. (2013). The state, control and algebraic variables are defined as:

$$x:=(q,\dot{q},C_\mathrm{L},\psi)\,, \quad u:=(\dot{C}_\mathrm{L},\dot{\psi})\,, \quad z:=\lambda\,, \tag{4}$$

with $q:=(q_0,q_1,q_2)\in\mathbb{R}^9$ the positions of the center point and the two wings, and $C_\mathrm{L}\in\mathbb{R}^2$ the lift coefficients and $\psi\in\mathbb{R}^2$ the roll angles of the two wings. The algebraic variables $\lambda\in\mathbb{R}^3$ are the Lagrange multipliers associated with the holonomic constraints

$$c(x,\theta):=\frac{1}{2}\begin{bmatrix} q_0^\top q_0-l_\mathrm{t}^2 \\ (q_1-q_0)^\top(q_1-q_0)-l_\mathrm{s}^2 \\ (q_2-q_0)^\top(q_2-q_0)-l_\mathrm{s}^2 \end{bmatrix}=0\,, \tag{5}$$

which impose that the node positions are consistent with the tether lengths $l_\mathrm{t}\in\mathbb{R}$ and $l_\mathrm{s}\in\mathbb{R}$ of the main and secondary tethers respectively. These parameters, together with the corresponding tether diameters $d_\mathrm{t}\in\mathbb{R}$ and $d_\mathrm{s}\in\mathbb{R}$, can be optimized over and are summarized in the parameter vector

$$\theta:=(l_\mathrm{t},l_\mathrm{s},d_\mathrm{t},d_\mathrm{s})\,. \tag{6}$$

Using the Lagrangian mechanics with index reduction approach proposed by Gros and Diehl (2013) and implemented by De Schutter et al. (2023b), we can derive the following equations of motion:

$$\begin{bmatrix} M & \nabla_q c \\ \nabla_q c^\top & 0 \end{bmatrix} \begin{bmatrix} \ddot{q} \\ \lambda \end{bmatrix} = F \tag{7}$$

with the mass matrix

$$M := \begin{bmatrix} \xi_\mathrm{t} + 2\xi_\mathrm{s} & \frac{1}{2}\xi_\mathrm{s} & \frac{1}{2}\xi_\mathrm{s} \\ \frac{1}{2}\xi_\mathrm{s} & \xi_\mathrm{s} + m_\mathrm{w} I_3 & 0 \\ \frac{1}{2}\xi_\mathrm{s} & 0 & \xi_\mathrm{s} + m_\mathrm{w} I_3 \end{bmatrix}, \tag{8}$$

where m_w is the wing mass and the terms $\xi_\mathrm{t} := \frac{1}{3}\mu_\mathrm{t} l_\mathrm{t} I_3$ and $\xi_\mathrm{s} := \frac{1}{3}\mu_\mathrm{s} l_\mathrm{s} I_3$ are used to describe the inertia of the tether. The density per unit length of the tether lengths is a function of the tether diameter, i.e. $\mu_\mathrm{t} := \rho_\mathrm{t} \frac{\pi d_\mathrm{t}^2}{4}$ and $\mu_\mathrm{s} := \rho_\mathrm{t} \frac{\pi d_\mathrm{s}^2}{4}$, with ρ_t the material density.

The force vector is given as

$$F := \begin{bmatrix} F_0 - \frac{3}{2} g(\xi_\mathrm{t} + 2\xi_\mathrm{s}) e_z \\ F_1 - g(m_\mathrm{w} + \frac{3}{2}\xi_\mathrm{s}) e_z \\ F_2 - g(m_\mathrm{w} + \frac{3}{2}\xi_\mathrm{s}) e_z \\ -\nabla_{\dot{q}} \dot{c}^\top \dot{q} \end{bmatrix} \tag{9}$$

with F_0, F_1 and F_2 the aerodynamic forces. In the implementation, Baumgarte stabilization is added in the last element of this vector, to ensure consistency of the solution in the context of periodic optimal control (Gros and Zanon, 2018).

2.2 Aerodynamics

To compute the aerodynamic forces, we assume a uniform free-stream wind speed $u_\infty \in \mathbb{R}^3$ and constant density $\rho \in \mathbb{R}$. Incorporating more realistic wind and density profiles as a function of flight altitude is considered straightforward and omitted here for simplicity.

The wake state $y(t,\cdot)$ induces an additional velocity field on top of the free-stream wind, which is evaluated at each of the wing positions $q_i(t)$, for $i \in \{1,2\}$:

$$u_{\mathrm{t},i}(q_i(t), y(t,\cdot)) := u_\infty + u_i^\mathrm{f}(q_i(t), y(t,\cdot)) \,. \tag{10}$$

For an explicit definition of the induced velocity functions u_i^f, we refer to Sect. 3.

The apparent wind speed seen by each wing is then given by

$$u_{\mathrm{a},i} := u_{\mathrm{t},i}(q_i(t), y(t,\cdot)) - \dot{q}_i(t) \,, \quad i \in \{1,2\} \,, \tag{11}$$

where, for notational simplicity, we further omit the explicit dependence on time.

Then, assuming no side-slip and direct control of the roll angle ψ_i of the wings, the resulting lift and drag forces are given by

$$F_{\mathrm{L},i} := \frac{1}{2}\rho S_{\mathrm{w}} C_{\mathrm{L},i} ||u_{\mathrm{a},i}||^2 (\cos(\psi_i) e_{\mathrm{L},i} - \sin(\psi_i) e_{\mathrm{T},i})$$

$$F_{\mathrm{D},i} := \frac{1}{2}\rho S_{\mathrm{w}} C_{\mathrm{D},i} ||u_{\mathrm{a},i}|| u_{\mathrm{a},i} \ ,$$

with the vectors $e_{\mathrm{L},i}$ and $e_{\mathrm{T},i}$ defined by

$$e_{\mathrm{T},i} := \frac{u_{\mathrm{a},i} \times e_{\mathrm{r},i}}{||u_{\mathrm{a},i} \times e_{\mathrm{r},i}||} \ , \quad e_{\mathrm{L},i} := \frac{e_{\mathrm{T},i} \times u_{\mathrm{a},i}}{||e_{\mathrm{T},i} \times u_{\mathrm{a},i}||} \ , \tag{12}$$

where $e_{\mathrm{r},i}$ is the tether direction:

$$e_{\mathrm{r},i} := \frac{q_i - q_0}{||q_i - q_0||} \ . \tag{13}$$

The aerodynamic drag coefficient includes the induced-drag term of an elliptical wing in straight flight:

$$C_{\mathrm{D},i} := C_{\mathrm{D},0} + \frac{C_{\mathrm{L},i}^2}{\pi \mathrm{AR}} \ , \tag{14}$$

with $C_{\mathrm{D},0}$ the parasitic drag and AR the aspect ratio. Note that the induced-drag term approximates the effect of the velocities induced by the part of the wake directly trailing the wing. This will be taken into account in the wake model in Sect. 3 so as to avoid double-counting, similar to (Trevisi et al., 2023).

The overall aerodynamic forces are given as

$$F_0 = F_{\mathrm{t},0} \tag{15}$$

$$F_i = F_{\mathrm{L},i} + F_{\mathrm{D},i} + F_{\mathrm{t},i} \ , \quad i \in \{1,2\} \ , \tag{16}$$

where $F_{\mathrm{t},i}$ are the tether drag forces, proportional to the tether lengths and diameters, properly distributed between the nodes. To simplify the exposition, we refer to (De Schutter et al., 2023b, Eq. 36) for the explicit expressions of the tether drag forces.

3 CONTINUOUS WAKE MODELING

We start our exposition of the continuous wake model by assuming that the two wings each have their own separate trailing wake described by the states $y_1(t,\tau) \in \mathbb{R}^{n_y}$ and $y_2(t,\tau) \in \mathbb{R}^{n_y}$, respectively, which are combined to form a total wake state:

$$y(t,\tau) := \begin{bmatrix} y_1(t,\tau) \\ y_2(t,\tau) \end{bmatrix} \ . \tag{17}$$

This wake state is the unique solution to the initial value problem defined by Eqs. 2 and 3. This solution can be explicitly expressed for each wake state $i \in \{1,2\}$ in terms of the functions f_i and g_i:

$$y_i(t,\tau) := g_i(x(t-\tau), y(t-\tau,\cdot)) + \int_0^{\tau} f_i(y(t-\tau,\cdot))\mathrm{d}s \ . \tag{18}$$

The forcing terms $f_i(t,\tau)$ can be used to model the wake convection and effects such as viscous dissipation, radial expansion, etc. Within the scope of this paper, we assume rigid convection with a velocity assigned at the moment of shedding. The functions g_i model the vortex properties at the moment of shedding, which depend on the system state and on the entire vortex structure itself (via the induced velocities).

The induced velocity evaluated at the position of each wing q_i is the superposition of the induced velocities of the individual wakes. These velocities are computed as an integral over the entire wake structure, assuming an infinitely long wake. For each wing, we ignore the induction of its own trailing wake less than a time T away, since this part is taken into account by the induced drag term. Therefore, we arrive at the following expression for the induced velocities for wing 1:

$$u_1^{\mathrm{f}}(q_1(t), y(t,\cdot)) := \int\limits_T^{\infty} u'(q_1(t), y_1(t,\tau))\mathrm{d}\tau + \int\limits_0^{\infty} u'(q_1(t), y_2(t,\tau))\mathrm{d}\tau\ , \tag{19}$$

and vice versa for wing 2.

Thus, to define a wake model in this framework, one must define a wake state representation y_i and the corresponding forcing and shedding functions f_i and g_i, and then model the induced velocity with the function u'.

3.1 Continuous vortex loop model

We propose to model each wake structure $y_i(t,\cdot)$ as a continuous trail of infinitely small vortex rectangles made up of infinitely thin vortex filaments with variable circulation strength $\Gamma_i(t,\tau)$, as shown in Fig. 1. The pair of chord-wise vortex filaments with infinitesimal length $\mathrm{d}s$ model the rolled-up wing tip vortices. The wake is shedded with the apparent wind speed, hence the infinitesimal length can also be written in function of τ as $\mathrm{d}s := ||u_{\mathrm{a},i}(t-\tau)||\mathrm{d}\tau$. We assume that these chord-wise filaments are located at a distance of $\frac{\pi}{4}b$ from each other (Gaunaa et al., 2020), symmetric relative to the rectangle center position $q_{\mathrm{v},i}(t,\tau)$. This distance equals the length of the pair of span-wise vortex filaments, which capture the shed vorticity caused by the variation of lift force over time. The orientation of the rectangles is determined by the normal unit vector $e_{\mathrm{n},i}(t,\tau)$ and chord-wise unit vector $e_{\mathrm{c},i}(t,\tau)$. The wake states are then defined as

$$y_i(t,\tau) := \begin{bmatrix} q_{\mathrm{v},i}(t,\tau) \\ \Gamma_i(t,\tau) \\ e_{\mathrm{n},i}(t,\tau) \\ e_{\mathrm{c},i}(t,\tau) \end{bmatrix}\ . \tag{20}$$

For the forcing term, we assume rigid downstream convection with a velocity $u_{\mathrm{conv},i}(y(t-\tau,\cdot)) \in \mathbb{R}^3$. This assumption implies that the shedded wake elements are transported without deformation or dissipation:

$$f_i(y(t-\tau,\cdot)) := \begin{bmatrix} u_{\mathrm{conv},i}(y(t-\tau,\cdot)) \\ 0_{7\times 1} \end{bmatrix}\ . \tag{21}$$

In reality, the wake evolution results from complex vortex–vortex interactions and self-induced deformations, which are computationally prohibitive to resolve explicitly. To account for these effects in a tractable manner, Sect. 4 introduces and compares three heuristic strategies for selecting the convection velocity.

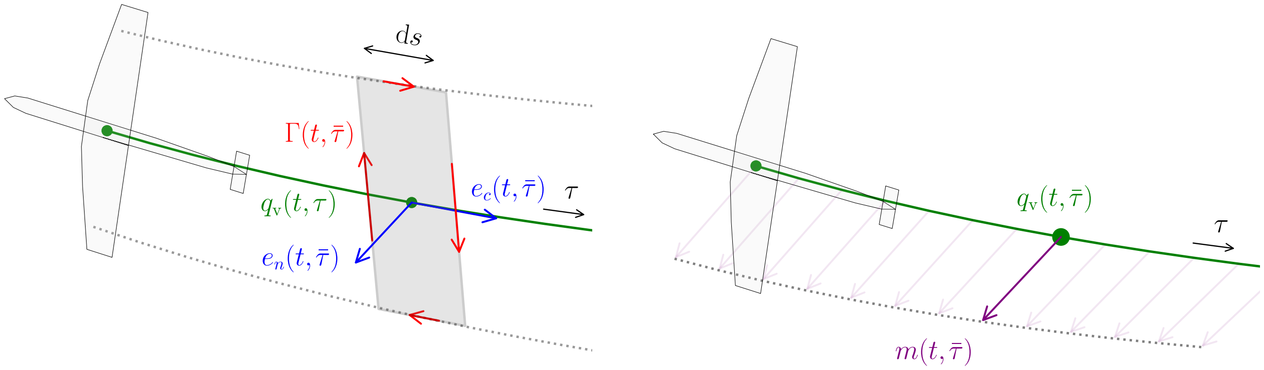

Figure 1. Illustration of the continuous wake representation based on rectangular vortex loops with the infinitesimally small width $\mathrm{d}s := ||u_\mathrm{a}(t-\tau)||\mathrm{d}\tau$, and of the wake representation based on a continuous trail of vortex dipoles.

The shedding laws g_i are defined such that the shedded rectangle center positions $q_{\mathrm{v},i}(t,0)$ coincide with the wings' aerodynamic center, here assumed equal to the center of mass positions $q_i(t)$. The trailing vortex strength $\Gamma_i(t,0)$ follows from the Kutta-Joukowski theorem (Gaunaa et al., 2020; Trevisi et al., 2023) for elliptic wings, while the rectangle unit vectors $e_{\mathrm{n},i}(t,0)$ and $e_{\mathrm{c},i}(t,0)$ are aligned with the lift force and apparent wind speed, respectively, which are orthogonal by definition:

$$g_i\left(x(t), y(t,\cdot)\right) := \begin{bmatrix} q_i(t) \\ \frac{2b}{\pi \mathrm{AR}} C_{\mathrm{L},i}(t)||u_{\mathrm{a},i}(t)|| \\ \frac{F_{\mathrm{L},i}(t)}{||F_{\mathrm{L},i}(t)||} \\ \frac{u_{\mathrm{a},i}(t)}{||u_{\mathrm{a},i}(t)||} \end{bmatrix}. \tag{22}$$

Finally, the induced velocity at a position $\hat{q} \in \mathbb{R}^3$ by an infinitesimally small rectangle per unit width $\mathrm{d}s = ||u_\mathrm{a}(t-\tau)||\mathrm{d}\tau$ is given by

$$u'(\hat{q}(t), y_i(t,\tau)) := \left.\frac{\mathrm{d}u_\mathrm{vl}(\hat{q}, y_i(t,\tau), \Delta s)}{\mathrm{d}\Delta s}\right|_{\Delta s = 0} ||u_{\mathrm{a},i}(t-\tau)||\,, \tag{23}$$

where the function u_vl computes the velocity induced by a rectangular vortex loop of chordwise extent Δs, obtained from the Biot–Savart law applied to its four bounding vortex filaments, as written out in Appendix A.

3.2 Continuous vortex dipole model

The symbolic complexity of Eq. 23 is relatively high, leading to expensive numerical derivatives and a high memory usage. This complexity can be reduced by applying a multi-pole expansion of the infinitesimal vortex loops and retaining only the leading non-vanishing term, which gives us a far-field approximation of the original induced velocity. This approximation can be interpreted as the induced velocity of a source dipole whose dipole moment is proportional to the enclosed area of the rectangular vortex loop.

Thus, we can also model the wake state as a continuous trail of vortex dipoles, visualized in Fig. 1 as well, which can be conveniently written as a function of the vortex loop state:

$$y^{\mathrm{d}}(y_i(t,\tau)) \coloneqq \begin{bmatrix} q_{\mathrm{v},i}(t,\tau) \\ m'_{\mathrm{d},i}(t,\tau) \end{bmatrix} \tag{24}$$

with the dipole moment per meter of trailing wake given by

$$m'_{\mathrm{d},i}(t,\tau) \coloneqq \Gamma_i(t,\tau) \cdot \frac{\pi b}{4} \cdot e_{\mathrm{n},i}(t,\tau)\ . \tag{25}$$

The induced velocity function of for the vortex dipole wake is given by the much simpler expression:

$$u'_{\mathrm{d}}(\hat{q}(t), y_i(t,\tau)) \coloneqq \frac{1}{4\pi} \frac{3r(r\cdot m'_{\mathrm{d},i}) - m'_{\mathrm{d},i}||r||^2}{||r||^5} ||u_{\mathrm{a},i}(t-\tau)|| \tag{26}$$

with

$$r \coloneqq \hat{q}(t) - q_{\mathrm{v},i}(t,\tau)\ . \tag{27}$$

Notice that the vortex dipole induced velocity is written explicitly as a function of the vortex loop state $y_i(t,\tau)$, so that the same state representation can be used for this model as well.

3.3 Continuous hybrid vortex model

With these two modeling options on the table, it is intuitive to conceptualize a hybrid wake model, consisting on the one hand of a costly vortex loop model that captures in detail the induction of the closest wake segments, and on the other hand the numerically cheaper vortex dipole moment to include the influence of the wake segments further downstream, as illustrated by Fig. 2.

We devise the hybrid model by splitting the integrals in Eq. 19 at the location $\tau = T_{\mathrm{A}}$ for the self-induced velocity of each wing, and at location $\tau = T_{\mathrm{B}}$ for the velocity induced by the wake of the other wing. For wing $i = 1$, this gives:

$$u_1^{\mathrm{f}}(q_1(t), y(t,\cdot)) \coloneqq \int_{T}^{T_{\mathrm{A}}} u'(q_1(t), y_1(t,\tau))\mathrm{d}\tau + \int_{T_{\mathrm{A}}}^{\infty} u'_{\mathrm{d}}(q_1(t), y_1(t,\tau))\mathrm{d}\tau + \int_{0}^{T_{\mathrm{B}}} u'(q_1(t), y_2(t,\tau))\mathrm{d}\tau + \int_{T_{\mathrm{B}}}^{\infty} u'_{\mathrm{d}}(q_1(t), y_2(t,\tau))\mathrm{d}\tau\ , \tag{28}$$

where the induced velocity for wing $i = 2$ is simply obtained by switching the wing indices for the variables q_i and y_i. Recall that for each wing we ignore the self-induced velocity for the first half-rotation interval with length T.

In this formulation, we can retrieve the full vortex-loop model ($T_{\mathrm{A}} = T_{\mathrm{B}} = \infty$), the full vortex dipole model ($T_{\mathrm{A}} = T, T_{\mathrm{B}} = 0$) or any variant in between.

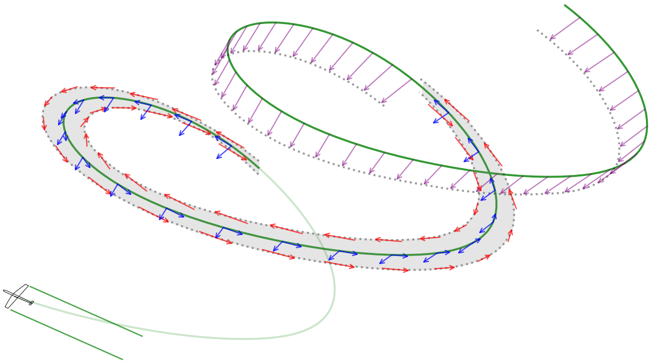

Figure 2. Illustration of the proposed hybrid rectangle-dipole model. The first half period of the trailing wake is modeled as a straight flight wake. Then, a full period is modeled using the continuous rectangle model, and all remaining periods are modeled using the continuous dipole model.

4 CONTINUOUS WAKE MODEL VALIDATION

To validate the new continuous wake formulation, we compare the model with the higher-fidelity, free-vortex software tool DUST (Tugnoli et al., 2021), an open-source, mid-fidelity aerodynamic solver specifically designed for analyzing complex 235 and non-conventional aircraft configurations. The software features a lifting-line method to compute the aerodynamic loads, coupled to a highly-resolved simulation of the wake using a vortex particle method that allows it to capture the complex vortex-to-vortex interactions that are largely ignored in the proposed optimization model.

4.1 Wing geometry and wake simulation in DUST

Two near-elliptic wings are generated using a parametric mesh with 40 discrete spanwise sections of the NACA 4421 air- 240 foil. The discretization introduces deviations from an ideal elliptical planform, leading to reduced aerodynamic efficiency. To account for this, a span efficiency factor e is incorporated into the induced drag model Eq. 14:

$$C_{\mathrm{D},i} := C_{\mathrm{D},0} + \frac{C_{\mathrm{L},i}^2}{\pi \mathrm{AR} e} \,, \tag{29}$$

and the corresponding trailing vortex strength in Eq. 22 is scaled accordingly:

$$\Gamma_i(t,0) := \frac{2b}{\pi \mathrm{AR} e} C_{\mathrm{L},i}(t) \| u_{\mathrm{a},i}(t) \| \,. \tag{30}$$

245 The efficiency factor, $e \approx 0.75$, is identified from a series of straight-flight DUST simulations across varying angles of attack. Inflow speeds are chosen to match the apparent wind conditions of the validation flight trajectory, ensuring consistency in Reynolds number. The factor e is then obtained by fitting Eq. 29 to the simulated drag polar.

To simulate the wake in DUST, we must prescribe a flight trajectory for the wings. To obtain a representative trajectory, we feed into DUST the optimal periodic wing position trajectories and orientations obtained by solving the optimization problem

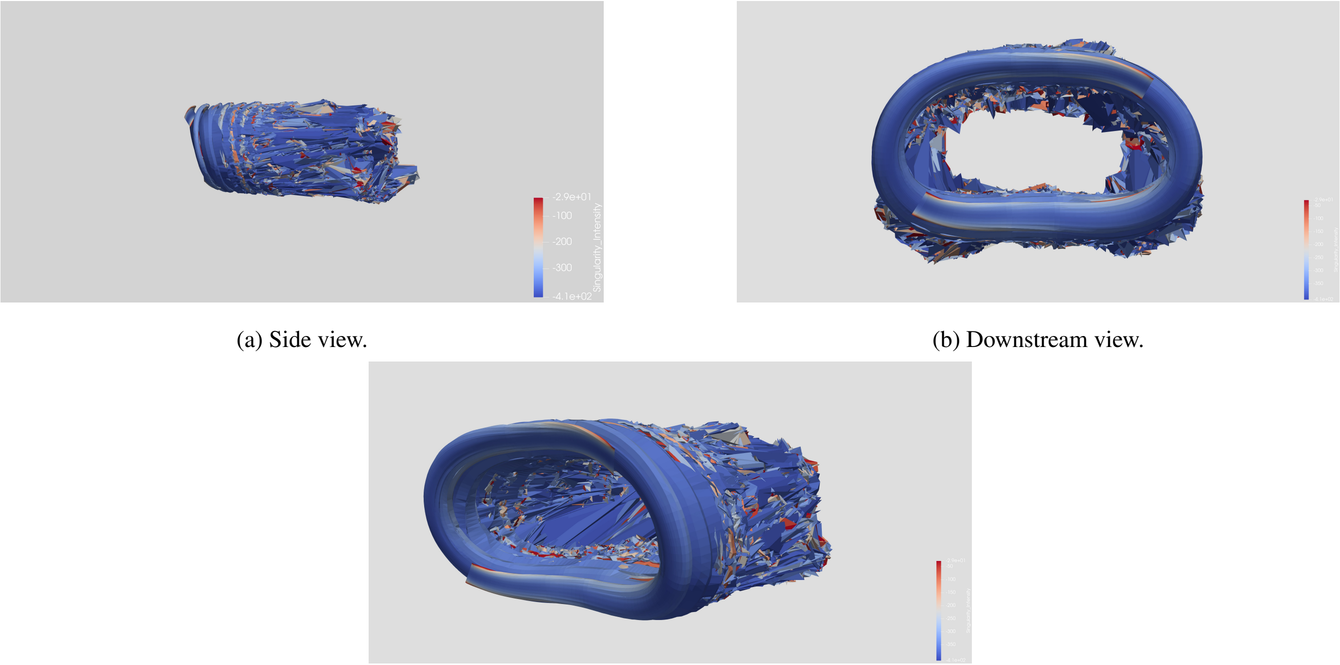

(a) Side view.

(b) Downstream view.

(c) 3D view.

Figure 3. DUST wake simulation result over 6.5 flight loops as visualized in Paraview.

defined by Eq. 59 from Sect. 5. One problem is that the optimal orientation trajectory by construction assumes zero angle-of-attack, since the optimization model assumes direct lift coefficient control. Therefore, in a preprocessing step, we apply a pitch correction to impose the angle of attack that would produce the same lift coefficient under the same conditions, using the simulated 3D lift polar.

The simulation is initialized in a vortex-free state, with vortex particles being shed during the simulation. We run the DUST simulation for 6.5 periods of the optimal state trajectory, to allow for the wake build-up to reach a steady state. Fig. 3 visualizes the simulation result, showing a distinct helicoidal wake structure in the first part of the wake, followed by an increasing break-up of this structure due to the vortex-to-vortex interactions. In postprocessing, we can retrieve the vortex particle trajectories, the induced velocity field at all time steps, and the aerodynamic loads obtained from the lifting-line approach. The toolchain to generate the necessary DUST input files as well as the input data and more detailed simulation settings (e.g. particle size, etc.) are made publicly available.

4.2 Wake convection comparison

To compare the DUST wake simulation with the proposed wake model, we evaluate the wake using the analytic solution defined by Eq. 18 and compute the induced velocities via Eq. 19 using a high-accuracy numerical integration scheme, running the integral up to 6.5 periods in the past. For the forcing term in Eq. 18, describing the wake convection, we consider three different convection velocity variants. For each variant, we obtain a different wake solution and a different time-dependent induced velocity field, which can be used to correct the aerodynamic loads obtained in the prescribed flight trajectory.

The first variant ("free") assumes no vortex-to-vortex interaction at all and prescribes convection with the free-stream wind velocity:

$$u_{\mathrm{conv},i}(y(t-\tau,\cdot)) := u_\infty \; . \tag{31}$$

The second variant ("far") assumes convection with reduced velocity due to far-wake induction at time of shedding, i.e.:

$$u_{\mathrm{conv},i}(y(t-\tau,\cdot)) := u_\infty + u_i^{\mathrm{f}}(q_{\mathrm{v},i}(t-\tau,0), y(t-\tau,0)) \; . \tag{32}$$

The third variant ("near") assumes convection with reduced velocity due to "near-wake" self-induction, as proposed by Trevisi et al. (2023), i.e.:

$$u_{\mathrm{conv},i}(y(t-\tau,\cdot)) := u_\infty - \frac{C_{\mathrm{L},i}\|u_{\mathrm{a},i}\|}{\pi \mathrm{AR} e} e_x \; . \tag{33}$$

Fig. 4 shows the position in the xz-plane of the vortex particles of the upper part of the wake. We compare this result with the predicted vortex-loop wake position trajectory and orientation, for each of the three variants. Firstly, it is visible that in the first, most influential part of the wake, the wake orientation and the distance between the tip vortices match very well with the DUST simulation. Further downstream, the models diverge slightly due to wake deformation and expansion. Regarding the convection velocity, the "free" variant strongly overestimates the convection velocity, whereas the "near" variant provides a strong underestimation. The "far" variant provides the best fit although some overestimation remains. In the remainder of this work, we apply the latter variant and delegate further improvements to future work.

4.3 Comparison of induced velocity and aerodynamic loads

For the purpose of optimal control, we are primarily interested in the induced velocity evaluated *at the wing position* and its effect on the aerodynamic loads. However, the DUST model does not differentiate between the induced velocity by the "far" wake structure and the local circulation around the wing that produces lift, as we do in the optimization model. Thus, to eliminate the local circulation effect around the wing, we probe the wind field by means of an imaginary pitot tube of length $l_{\mathrm{p}} = 0.9b$ pointing forward in chord direction. For the vortex-loop model, we evaluate the induced velocity at the same location:

$$\hat{u}_i^{\mathrm{f}}(t) := u_i^{\mathrm{f}}(q_i(t) + l_{\mathrm{p}} e_{\mathrm{c},i}(t), y(t,\cdot)) \; , \tag{34}$$

with $e_{\mathrm{c},i}$ the pitch-corrected chord-wise body frame vector.

Fig. 5 (left) shows the component-wise comparison of the measured induced velocity, normalized with the free-stream wind speed. For the first half rotation, the DUST induced velocity is almost zero, as the wake has not developed yet. After that, the magnitude of the induced velocity increases rotation after rotation as the wake builds up until it reaches a steady-state. When comparing the induced velocities at the end of the DUST simulation with those from the periodic vortex-loop simulation, we

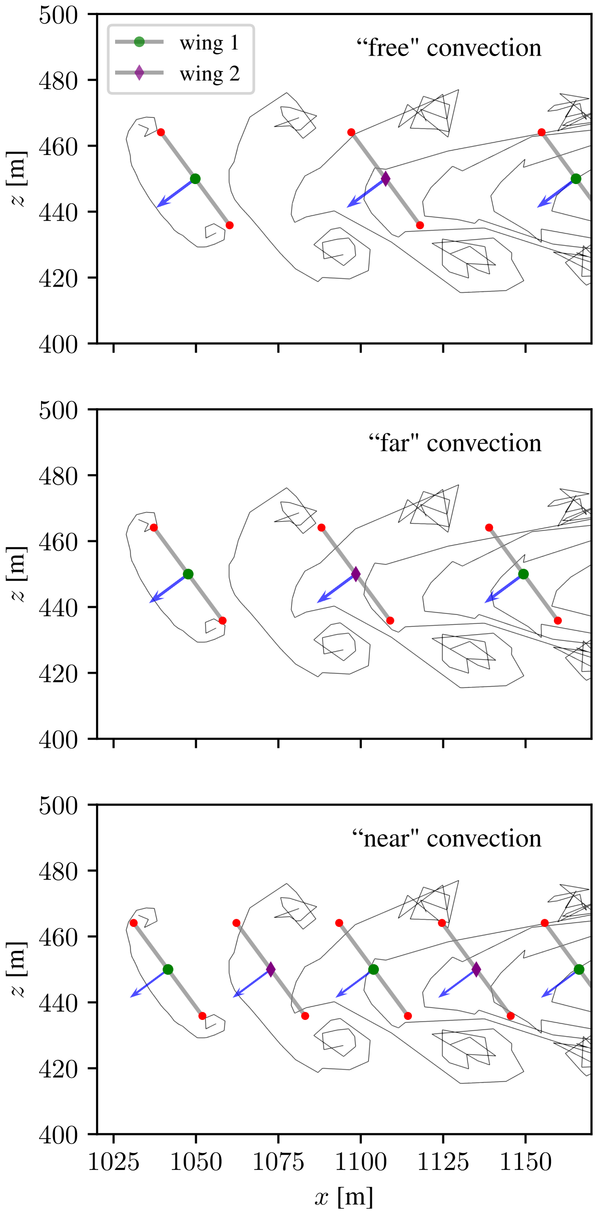

Figure 4. Comparison of snapshots of the vortex-loop wake position and orientation for the three convection velocity variants and the DUST simulation, for fully developed wakes of 6.5 periods and at the intersections with the xz-plane.

https://doi.org/10.5194/wes-2025-275
Preprint. Discussion started: 16 January 2026

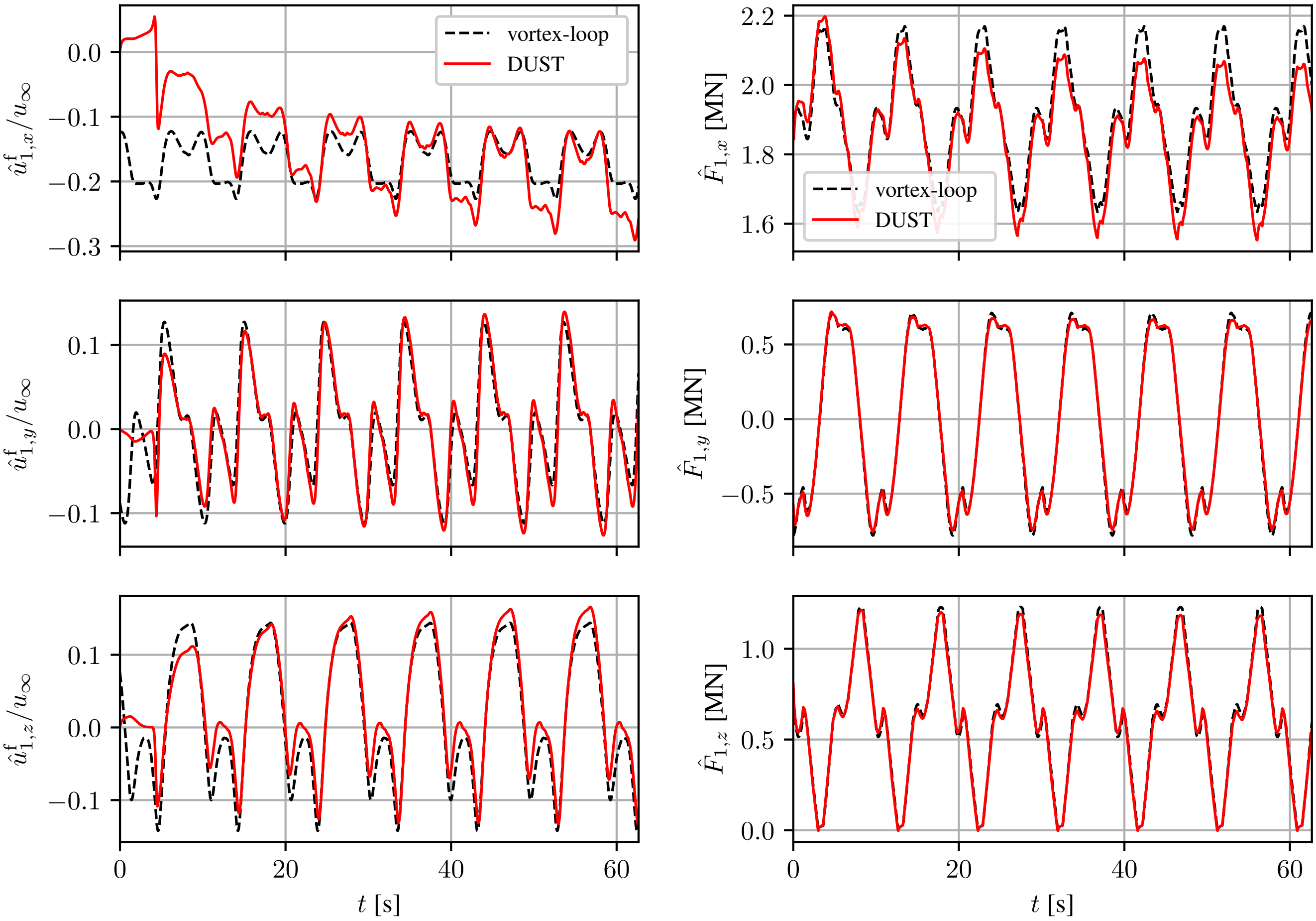

Figure 5. Comparison of the induced velocity (left) and aerodynamic forces (right) components corresponding to the continuous vortex-loop and DUST simulations. Note that the vortex-loop profiles are periodic and correspond to a developed wake of 6.5 periods, whereas the DUST simulation starts with no wake history and thus we can observe the wake build-up.

see a very good agreement of the y- and z-components. Also for the x-component, the vortex-loop model captures the unsteady nature of the wake very well. However, due to the overestimation in convection velocity, the vortex-loop model underestimates the induced velocity by up to $25\,\%$ in the dominant x-direction.

Fig. 5 (right) shows the effect of this mismatch on the different components of the aerodynamic loads $\hat{F}_i := F_{\mathrm{L},i} + F_{\mathrm{D},i}$. Again, we have a very good agreement in the y- and z-directions. In the x-direction, the induced velocity mismatch leads to an overestimation of the angle-of-attack and consequently an overestimation of the loads up to $5\,\%$.

In summary, the vortex-loop model provides a strong match with the DUST benchmark. The y- and z-components of the induced velocities are captured with high accuracy. In the dominant x-direction there is a moderate mismatch, mainly resulting from the limitations of the convection model. Nevertheless, it is important to note that the model reproduces very well the unsteady and non-axisymmetric nature of the wake that conventional approaches fail to represent.

4.4 Comparison of induced velocity field

For optimization purposes, it is not only important to have a good model for the induced velocity evaluated at the wing position, but also in its surrounding neighborhood. Therefore, we also compare the induced velocity field of the vortex-loop model with that of DUST in the region around the optimal trajectory. Figs. 6 and 7 plot the induction factor in x- and z-direction at the same time point t' as in Fig. 4, taking into account the contribution of the entire wake. In accordance with the findings in the previous section, we can discern a slight overall underestimation of the induced velocities in front of the wake. Nevertheless, the qualitative fit is very good in both directions. Fig. 8 shows another snapshot of the induction factor in x-direction in a plane perpendicular to the average main tether direction, located at the average wings' position, allowing us to draw similar conclusions in the region normal to the tether.

5 Efficient problem formulation

After the validation of the proposed wake model in the previous section, the goal of this section is to use this model in optimal control problem (OCP) formulations and outline the transcription and approximation steps taken to arrive at an efficient implementation. Therefore we first formulate the envisaged PDE-based optimal control problem in continuous-time. Then we propose a wake discretization strategy using auxiliary wake states. This approach transcribes the PDE optimization problem into a standard continuous-time OCP with state jump constraints for the wake states. Finally, we introduce further simplifications to render the final OCP numerically tractable.

5.1 PDE optimal control problem

For all types of crosswind kite systems, the challenge is to compute periodic flight orbits that maximize a certain averaged performance index. In the AWE case, the performance index is typically the power output. For the atmospheric airborne actuator case, as well as for the ship-towing case, the tether pulling force is to be maximized:

$$l(x(t),u(t),z(t),\theta) := -F_{\mathrm{t}}(t) := -\lambda_0(t) l_{\mathrm{t}} \,, \tag{35}$$

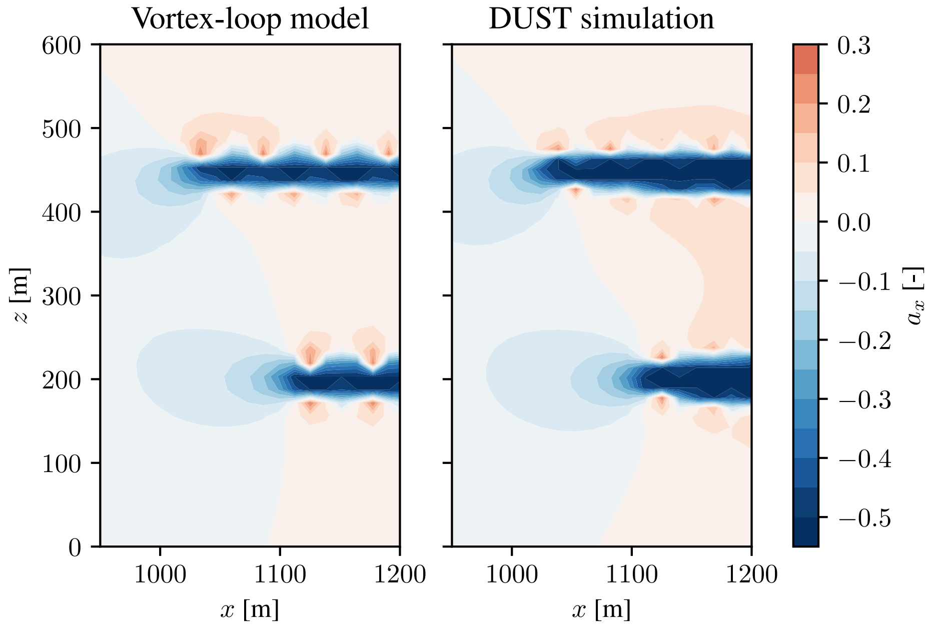

Figure 6. Validation of the simulated induction factor fields ($a_x := \frac{u_x^{\mathrm{f}}(q,y(t,\cdot))}{u_\infty}$) in the plane defined by $y = 0$. Note that we include the "near-wake" part of the vortex-loop induction, i.e., the first integral in Eq. 19 starts at $\tau = 0$.

while satisfying the following constraints

$$h(x(t),u(t),z(t),\theta) := \begin{bmatrix} \pi d_{\mathrm{t}}^2 \sigma_{\mathrm{max}} - 4F_{\mathrm{t}}(t) \\ (2.2b)^2 - (q_2 - q_1)^\top (q_2 - q_1) \\ \nu - \nu_{\mathrm{min}} \\ \nu_{\mathrm{max}} - \nu \end{bmatrix} \geq 0\,, \tag{36}$$

which impose a maximum tether stress constraint with $\sigma_{\mathrm{max}} = 2.4\,\mathrm{GPa}$, an anticollision constraint, and the bounds on the variables $\nu := (x,u,z,\theta,T)$ summarized in Table 1.

Further, since the optimal state trajectory will be periodic, the wake state will be periodic in t as well. Therefore we can reformulate the wake transport equation as

$$\frac{\mathrm{d}y}{\mathrm{d}t}(t,\tau) + \frac{\mathrm{d}y}{\mathrm{d}\tau}(t,\tau) = f(y([t-\tau],\cdot)\,, \tag{37}$$

https://doi.org/10.5194/wes-2025-275
Preprint. Discussion started: 16 January 2026

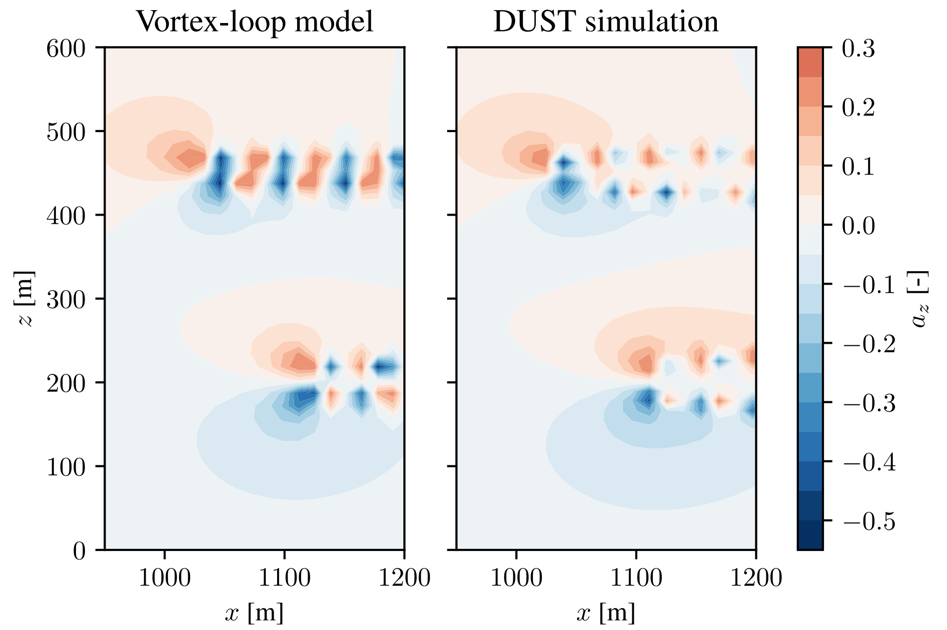

Figure 7. Validation of the simulated induction factor fields ($a_z := \frac{u_z^{\mathrm{f}}(q, y(t,\cdot))}{u_\infty}$) in the plane defined by $y = 0$. Note that we include the "near-wake" part of the vortex-loop induction, i.e., the first integral in Eq. 19 starts at $\tau = 0$.

Table 1. System variable bounds

Description	Symbol	Min	Max	Units
Tether length	l_{t}	10.0	700.0	m
Flight altitude	q_{z}	200.0	-	m
Time period	T	1.0	10.0	s
Tether multiplier	λ	0	∞	$\mathrm{N\,m^{-1}}$
Lift coefficient	C_{L}	0	1.0	-
Lift coefficient rate	$\dot{C}_{\mathrm{L}}$	-5.0	5.0	s^{-1}
Roll angle	ψ	-30.0	30.0	deg
Roll angle rate	$\dot{\psi}$	-5.7	5.7	deg/s

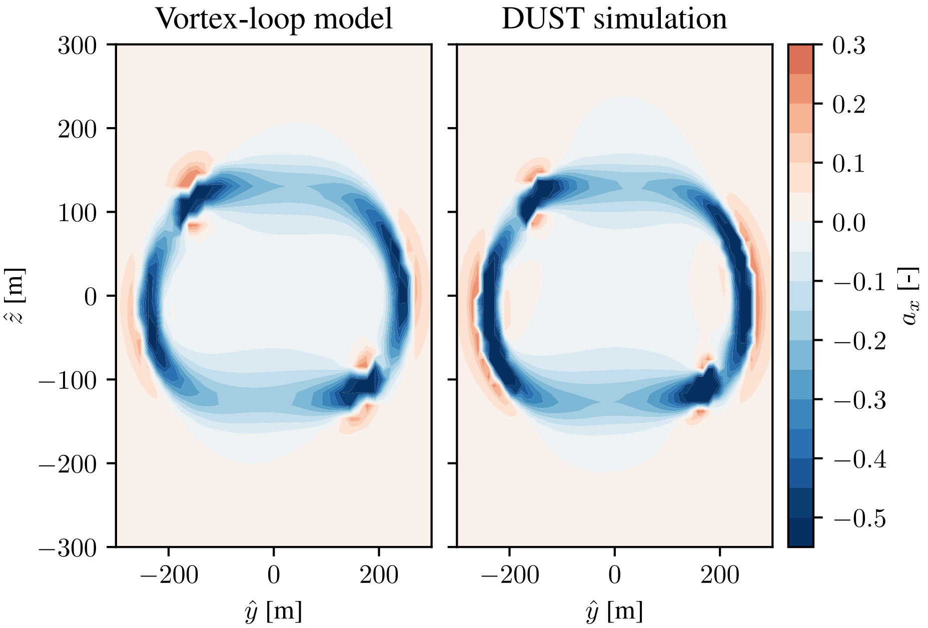

Figure 8. Validation of the simulated induction factor fields (a_x as in Fig. 6) in the $\hat{y}\hat{z}$-plane perpendicular to the average main tether direction, located at the average wings' position.

with the modulo operator $[t] := t \bmod T$, so that the wake state only needs to be tracked for $t \in [0,T]$. Using this reformulation, we can formulate the following continuous and periodic PDE optimal control problem:

335
$$\begin{aligned}
\underset{\substack{x(\cdot),u(\cdot),z(\cdot)\\ y(\cdot,\cdot),\theta,T}}{\text{minimize}} \quad & \frac{1}{T}\int_0^T l(x(t),u(t),z(t),\theta)\mathrm{d}t \\
\text{subject to} \quad & F(x(t),\dot{x}(t),u(t),z(t),y(t,\cdot),\theta) = 0 \quad t \in [0,T], \\
& h(x(t),u(t),z(t),\theta) \geq 0, \quad t \in [0,T], \\
& \frac{\mathrm{d}y}{\mathrm{d}t}(t,\tau) + \frac{\mathrm{d}y}{\mathrm{d}\tau}(t,\tau) - f(y([t-\tau],\cdot)) = 0 \quad t \in [0,T], \\
& \qquad \tau \in [0,\infty), \\
& y(t,0) - g(x(t),y(t,\cdot)) = 0 \quad t \in [0,T], \\
& x(0) - x(T) = 0\,.
\end{aligned} \tag{38}$$

This problem is infinite-dimensional both in t and τ and numerically intractable. The first step is to transcribe the problem into a form that is only infinite-dimensional in t.

https://doi.org/10.5194/wes-2025-275
Preprint. Discussion started: 16 January 2026

5.2 Wake transcription

We propose to discretize the wake on a uniform grid of M points in the τ-space:

$$0 < \tau_1 < \ldots < \tau_j < \ldots < \tau_M < T, \tag{39}$$

and introduce on this grid the periodic wake state

$$y^{(j)}(t) \approx y(t, t+\tau_j)\ , \tag{40}$$

which approximately tracks the evolution of points j in the wake, originating at a time $t = [-\tau_j] = T - \tau_j$, that are convected away as time progresses. We can derive that the derivative of this wake state should approximate the forcing term in Eq. 37:

$$\dot{y}^{(j)}(t) \approx f(y([-\tau_j], \cdot))\ , \tag{41}$$

and we model its origination as an impulsive event along its periodic trajectory:

$$y^{(j)}([-\tau_j]^+) \approx g(x([-\tau_j]^-), y([-\tau_j]^-, \cdot))\ . \tag{42}$$

Notice how in Eq. 41, the individual derivatives each depend on the entire wake history, which is counterproductive as it produces cross-couplings over different time instances. To arrive at a more classical state equation, we propose to extend the wake states with these derivatives, and collect both in one overall wake state:

$$Y(t) := \begin{bmatrix} y^{(1)}(t) \\ \dot{y}^{(1)}(t) \\ \vdots \\ y^{(M)}(t) \\ \dot{y}^{(M)}(t) \end{bmatrix}\ . \tag{43}$$

The state equation is trivially given by (assuming rigid convection):

$$\dot{Y}(t) = F_Y(Y(t)) := \begin{bmatrix} \dot{y}^{(1)}(t) \\ 0 \\ \vdots \\ \dot{y}^{(M)}(t) \\ 0 \end{bmatrix}\ , \tag{44}$$

and the impulse effect can be written as

$$Y([-\tau_j]^+) = G_j(x([-\tau_j]^-), Y([-\tau_j]^-))\ , \tag{45}$$

with the impulse function defined as

$$G_j(x(t), Y(t)) := \begin{bmatrix} y^{(j)}(t) - \tilde{g}(x(t), Y(t)) \\ \dot{y}^{(j)}(t) - \tilde{f}(Y(t)) \end{bmatrix}\ . \tag{46}$$

Here, the functions $\tilde{f}$ and $\tilde{g}$ are defined by replacing the induced velocity expression in the functions f and g as follows:

$$u^{\mathrm{f}}_1(q_1, y(t,\cdot)) \approx \tilde{u}^{\mathrm{f}}_1(q_1, Y(t)) \,. \tag{47}$$

where the function $\tilde{u}^{\mathrm{f}}_1$ is obtained via a numerical integration scheme based on the discretized wake state $Y(t)$ (see below).

To simplify notation, we further only consider the hybrid model where each wing experiences its own induction through the dipole model only ($T_\mathrm{A} = T$) and the induction caused by the other wing's wake only for one full rotation with the vortex-loop model ($T_\mathrm{B} = 2T$). As we will discuss later in Sect. 6, this model choice is sufficiently accurate compared to the full vortex-loop model. Nevertheless, the following developments can be worked out for all different hybrid variants as well.

The integrals in Eq. 28 extend over an infinite horizon in the τ-domain, whereas the wake state $Y(t)$ retains only a single period T of past history. However, using the analytic wake solution formula Eq. 18, and exploiting the wake periodicity, we can look further in the past by introducing (e.g., for a wing "i", *as seen by wing "1"*) a finite number N_d of "duplicate" wake states $y^{(j)}_{1i,d}(t)$, based on the tracked wake states $y^{(j)}_i(t)$, that are convected downwind for d periods of duration T:

$$y^{(j)}_{1i,d}(t) := y^{(j)}_i(t) + (d + p^{\mathrm{n}}_{1i}(t,\tau_j)) T \dot{y}^{(j)}_i(t) \tag{48}$$

Notice that we also introduced the "near wake parameter" $p^{\mathrm{n}}_{1i}(t,\tau_j)$, which makes sure that we only consider the duplicates of those wake states that are in the near wake region at the current time point t. Formally, this parameter is defined as (for $i \in \{1,2\}$):

$$p^{\mathrm{n}}_{ii}(t,\tau_j) := \begin{cases} 1 & \text{if } t \geq [-\tau_j] \,, \\ 0 & \text{if } t < [-\tau_j] \,, \end{cases} \tag{49}$$

and

$$p^{\mathrm{n}}_{12}(t,\tau_j) := \begin{cases} 0 & \text{if } t \geq [-\tau_j] \,, \\ 1 & \text{if } t < [-\tau_j] \,, \end{cases} \tag{50}$$

and $p^{\mathrm{n}}_{21} = p^{\mathrm{n}}_{12}$.

Based on the introduced duplicate wake states, the induced velocity for wing 1, using the hybrid model, can be computed numerically as follows using the midpoint integration rule:

$$\tilde{u}^{\mathrm{f}}_1(q_1(t), Y(t)) := \sum_{i=1}^{2} \left(\sum_{d=1}^{N_\mathrm{d}} \sum_{j=1}^{M} u'_\mathrm{d}(q_1(t)), y^{(j)}_{1i,d}(t))\Delta\tau + \sum_{j=1}^{M} u'(q_1(t)), y^{(j)}_{1i,0}(t))\Delta\tau \right) \,. \tag{51}$$

The induced velocity $\tilde{u}^{\mathrm{f}}_2(q_2(t), Y(t))$ for wing 2 is simply obtained by change of index.

5.3 Window of influence

At every time instance t, the induced velocities defined by Eq. 51 depend on the entire wake state $Y(t)$. This results in a dense sensitivity structure for the dynamics, which ultimately leads to a high memory usage, and more time spent in the linear solver

https://doi.org/10.5194/wes-2025-275
Preprint. Discussion started: 16 January 2026

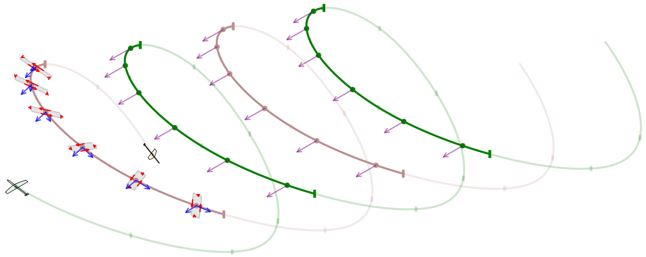

Figure 9. Illustration of the proposed fixed window of influence for a dual-kite system with $N = 4$, $M = 8$, $N_\mathrm{d} = 3$, $N_\mathrm{f} = 1$

backend of the optimization solver. Experience showed that it is crucial to exploit the fact that the influence of each wake element at any given time depends on how close it is to the position of the wing at that time. Therefore, the contribution of more remote elements can be neglected at a low loss of accuracy. We implement this by assigning to each wing a moving *window of influence*.

To this end, we divide the time grid in N equidistant intervals

$$0 = t_0 < \ldots < t_k < \ldots < t_N = T \;, \tag{52}$$

and as the wing passes through each interval, we only take into account the wake segments that originate from that particular interval and the neighboring N_f intervals, as illustrated by Fig. 9.

At a given time point t, we determine the current interval k as

$$k := \left\lfloor \frac{Nt}{T} \right\rfloor \tag{53}$$

and the window that is taken into account in interval k is defined by the boundaries

$$\underline{T}_{\mathrm{f},k} := t_k - N_\mathrm{f}\frac{T}{N} \;, \tag{54}$$

$$\bar{T}_{\mathrm{f},k} := t_{k+1} + N_\mathrm{f}\frac{T}{N} \;. \tag{55}$$

We then introduce the “far wake parameters”

$$p^\mathrm{f}_{ii}(t,\tau_j) := \begin{cases} 1 & \text{if } [-\tau_j] \in \left[\underline{T}_{\mathrm{f},k}, \bar{T}_{\mathrm{f},k}\right] \;, \\ 0 & \text{otherwise} \;, \end{cases} \tag{56}$$

and

$$p^\mathrm{f}_{12}(t,\tau_j) := \begin{cases} 1 & \text{if } \{-\tau_j, 2T-\tau_j\} \cap \left[\underline{T}_{\mathrm{f},k}, \bar{T}_{\mathrm{f},k}\right] \neq \emptyset \\ 0 & \text{otherwise} \;, \end{cases} \tag{57}$$

with $p^{\mathrm{f}}_{21} = p^{\mathrm{f}}_{12}$. This parameter is then used to switch on and off the contribution of the individual wake elements, e.g. for wing $i = 1$:

$$\tilde{u}^{\mathrm{f}}_1(q_1(t),Y(t)) := \sum_{i=1}^{2}\left(\sum_{d=1}^{N_\mathrm{d}}\sum_{j=1}^{M} p^{\mathrm{f}}_{1i}(t,\tau_j)u'_\mathrm{d}(q_1(t)),y^{(j)}_{1i,d}(t))\Delta\tau + \sum_{j=1}^{M} p^{\mathrm{f}}_{1i}(t,\tau_j)u'(q_1(t)),y^{(j)}_{1i,0}(t))\Delta\tau\right). \tag{58}$$

The parameter N_f can then be tuned in numerical experiments to achieve the best trade-off between accuracy and computation time.

5.4 Continuous-time OCP Implementation

By transcribing the wake model as detailed above, we can reformulate the PDE optimal control problem from Eq. 38 into the more standard continuous-time formulation:

$$\begin{aligned}
&\underset{\substack{x(\cdot),u(\cdot),z(\cdot)\\ Y(\cdot),\theta,T}}{\text{minimize}} \quad \frac{1}{T}\int_0^T l(x(t),u(t),z(t),\theta)\mathrm{d}t\\
&\text{subject to} \qquad \tilde{F}(x(t),\dot{x}(t),u(t),z(t),Y(t),\theta) = 0 \quad t\in[0,T],\\
&\qquad\qquad h(x(t),u(t),z(t),\theta) \geq 0,\ \ t\in[0,T],\\
&\qquad\qquad \dot{Y}(t) - F_Y(Y(t)) = 0,\ \ t\in[0,T],\\
&\qquad\qquad Y([\tau_j]^+) - G_j(x(([\tau_j]^-),Y([\tau_j]^-)) = 0,\ \ j\in\mathbb{I}_1^M,\\
&\qquad\qquad x(0) - x(T) = 0,\\
&\qquad\qquad Y(0) - Y(T) = 0\,.
\end{aligned} \tag{59}$$

where the dynamics $\tilde{F}$ are obtained by inserting the induced velocity expression from Eq. 58 into the dynamics F.

Specifically for the dual-kite configuration, simulating a full orbit reveals that the two airfoils follow nearly identical trajectories. To eliminate this redundancy, the dynamics are instead integrated over half an orbit, with the optimal control problem formulated to enforce half-periodicity by matching the end state of each kite to the initial state of the other, as proposed by Zanon et al. (2013). Thereby, the problem size is halved and the time variable T automatically becomes the desired half-rotation near-wake cut-off time period.

We then transcribe this problem into a nonlinear program (NLP) using a direct collocation approach. We choose the number of collocation intervals equal to the number of intervals N considered by the finite window approach. Each interval consists of four RadauIIa collocation points, as detailed by De Schutter et al. (2023b). The transcription includes a time transformation approach to deal with the variable time grid. Additionally, the computational performance benefits from an additional lifting of the induced velocities as algebraic variables to reduce nonlinearity and symbolic complexity. We implemented this problem in the open-source framework `AWEbox` (De Schutter et al., 2023b), which relies on the symbolic framework `CasADi` (Andersson et al., 2019) for automatic differentiation and the interface to the NLP solver `IPOPT` (Wächter and Biegler, 2006), using `MA57` (HSL, 2011) as the linear solver backend. The problem is solved on an Intel Core i7 2.5 Ghz, 16GB RAM.

https://doi.org/10.5194/wes-2025-275
Preprint. Discussion started: 16 January 2026

6 Numerical example

6.1 OCP solution comparison

To illustrate the proposed approach, we solve the OCP from Eq. 59 for a dual-kite system using the numerical parameters provided by Table 2. Initially, the wake discretization parameters are chosen so that a good fit with the post-ex analytic wake solution is achieved. Table 3 summarizes the chosen parameters.

Fig. 10 shows the resulting optimal flight trajectory in comparison to the case where no induction (NI) model is included. Note that the corresponding optimal wake state, induced velocities and aerodynamic forces have already been discussed in Sect. 3 and shown in Fig. 3 to Fig. 8. Table 4 summarizes the main results of the optimization. The chosen induction model parametrization increases the computation time per iteration t_{CPU} by a factor 16 compared to the NI case.

The optimizer increases the secondary tether lengths from 2.5 in the NI case to almost ten wing spans. While this leads to higher tether drag losses, it allows the system to fly longer time periods T, which creates a larger convection distance between the system and its wake. Hence, the induction losses are reduced up to the point where the tether drag becomes dominant.

Also, because the available wind speed is reduced, the wings fly slower and experience a $30\,\%$ lower airspeed compared to the NI case, and they produce $55\,\%$ less average tether force. As a result, the tether diameters can be dimensioned smaller, which helps to dampen the effect of the increased tether drag. In conclusion, both the optimal design and performance of the considered system are highly sensitive to the inclusion of induction effects.

6.2 Discretization sensitivity

To assess the trade-off between computational effort and solution accuracy, we evaluate the impact of coarser wake parametrizations relative to the reference case. Each discretization parameter (M, N_{d}, and N_{f}) is independently reduced while the others are held at their reference values. For each configuration, the optimal control problem is re-solved, and the resulting computational cost and accuracy are compared against the reference solution. The error E is defined relative to the reference solution so as to capture both the accuracy of the cost as that of the optimal design:

$$E := \left\| \begin{bmatrix} \frac{\bar{F}_{\mathrm{t}}^{*} - \bar{F}_{\mathrm{t,ref}}^{*}}{\bar{F}_{\mathrm{t,ref}}^{*}} & \frac{\theta^{*} - \theta_{\mathrm{ref}}^{*}}{\theta_{\mathrm{ref}}^{*}} \end{bmatrix} \right\| \qquad (60)$$

Fig. 11 shows the trade-off between computational cost and accuracy across the tested wake parametrizations, including the no-induction (NI) case.

As the number of wake duplicates is reduced ($N_{\mathrm{d}} \downarrow$), the solution accuracy is significantly affected. In particular, whether to include the first duplicate ($N_{\mathrm{d}} = 1$) or not has a large influence. The computation time on the other hand, is hardly affected, as the duplicates do not change the NLP dimensions or sparsity pattern. This suggests that the number of duplicates should be carefully selected, but that they can be added at little additional computational cost.

Reducing the window of influence size ($N_{\mathrm{f}} \downarrow$) significantly decreases computation time, as the resulting NLP becomes increasingly sparse. However, when the window is chosen too small (in this case, $N_{\mathrm{f}} = 0$), solution accuracy deteriorates, and a spurious trajectory is obtained that performs even worse than the no–induced-wake (NI) case. These observations justify the

Table 2. Kite system model parameters used in the numerical example.

Description	Symbol	Value	Dim.
Wing mass	m_w	4000	kg
Wing area	S_w	200	m^2
Aspect ratio	AR	10	-
Wing span	b	44.72	m
Tether material density	ρ_t	1464.2	$\mathrm{kg\,m^{-3}}$
Air density	ρ	1.225	$\mathrm{kg\,m^{-3}}$
Free-stream wind velocity	u_∞	$\begin{bmatrix}12 & 0 & 0\end{bmatrix}$	$\mathrm{m\,s^{-1}}$

introduction of a finite window of influence and highlight N_f as a key discretization parameter governing the balance between numerical efficiency and model fidelity.

Finally, reducing the number of wake elements ($M \downarrow$) leads to a moderate decrease in both computation time and solution accuracy, indicating that relatively coarse discretizations can still yield meaningful results. However, for small M, oscillations appear in the time-resolved profile of the induced velocity, as illustrated by Fig. 12. This behavior arises from the dependence of the induced velocity on the wing position: when the wing passes directly over a wake element, the induced velocity reaches a peak and subsequently drops to a minimum halfway to the next element. Consequently, the integration error in Eq. 58 is position-dependent and sensitive to the choice of collocation grid in the time-continuous OCP Eq. 59. A potential remedy would be to implement a continuously moving window of influence that tracks the wing position, rather than the discrete interval-to-interval update scheme used here. While this would increase the computational complexity of the induced-velocity evaluation, it could provide a consistent integration accuracy especially for small values of M. Such an extension is left for future work.

Fig. 12 also shows the induced velocity from the analytic vortex-loop solution evaluated at the optimal solution for $M = 24$. The induced velocity computed using the hybrid wake representation (comprising a single layer of vortex loops followed by dipole elements) shows good agreement with the one obtained from the full vortex-loop formulation, thereby justifying the use of dipoles for far-convected wake elements in this case. For applications involving larger convection distances, as are likely to occur for the case of single-kite AWE systems, the accuracy of the hybrid approximation is expected to improve further.

Based on the sensitivity analysis above, a new parametrization, denoted as “A”, is selected by choosing for each discretization parameter the lowest value that still yields a relative error $E < 5\,\%$. This configuration represents a Pareto-efficient trade-off between computational cost and model fidelity among the tested cases. At point A, it also holds that $E < 5\,\%$, while the average computation time per iteration is now only a factor 3 more expensive than the NI case, which comes with a value of $E = 145\,\%$. In conclusion, when very high accuracy is not required—such as during design exploration or when other modeling errors are of comparable magnitude—there exist parametrizations that provide approximate solutions of the PDE OCP from Eq. 38 with only a moderate increase in computation time compared to the NI case.

https://doi.org/10.5194/wes-2025-275
Preprint. Discussion started: 16 January 2026

Table 3. Wake discretization parameters

Description	Symbol	Ref. case	A case
Number of discrete wake elements	M	24	8
Number of wake duplicates	N_d	3	2
Window of influence size	$2N_\mathrm{f}+1$	9	3

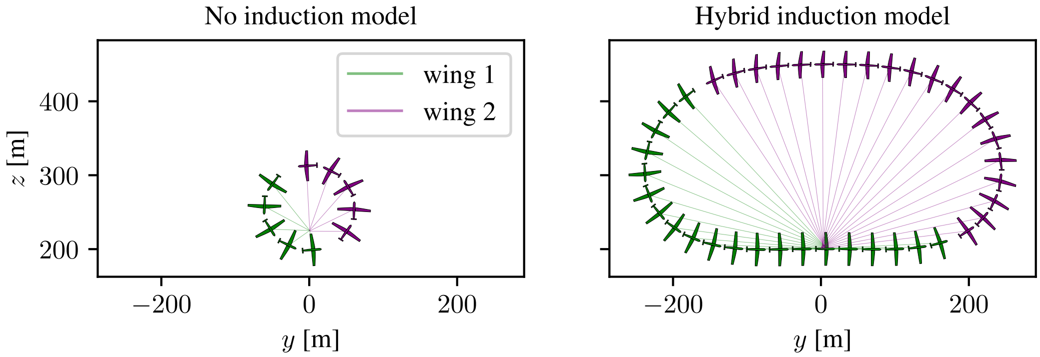

Figure 10. Optimal flight trajectories corresponding to the solution of the OCP from Eq. 59, where the induction is discarded (left) and where the hybrid induction model is used (right).

Table 4. Optimal solution indicators and computation time.

Description	Symbol	No induction	Hybrid induction	Dimension
Average tether force	$\bar{F}_\mathrm{t}$	8822.8	3967.5	kN
Average airspeed	$\bar{u}_\mathrm{a}$	189.8	132.1	$\mathrm{m\,s^{-1}}$
Half time period	T	1.0	4.4	s
Main tether length	l_t	700.0	700.0	m
Secondary tether length	l_s	113.5	439.3	m
Main tether diameter	d_t	68.7	47.8	mm
Secondary tether diameter	d_s	53.0	35.1	mm
CPU time per iteration	t_CPU	0.15	2.35	s

https://doi.org/10.5194/wes-2025-275
Preprint. Discussion started: 16 January 2026

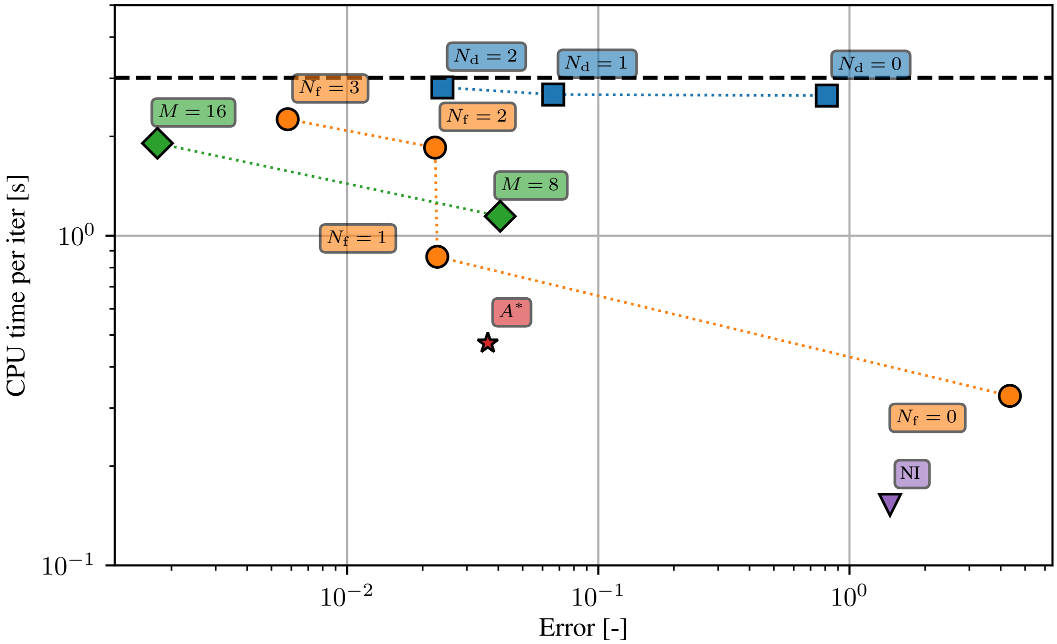

Figure 11. Comparison of CPU time vs. relative error E of different wake parameterizations compared to the reference parameterization (CPU time given by dashed black line).

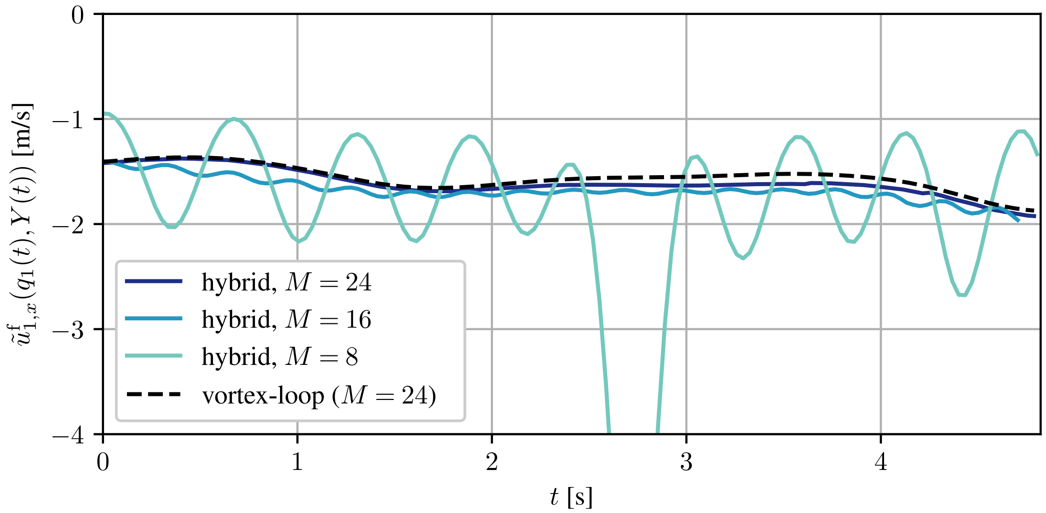

Figure 12. Time-resolved optimal far wake induction profile (x-component), evaluated at wing 1, for different numbers of wake elements M, compared with the exact vortex-loop solution evaluated for $M = 24$.

https://doi.org/10.5194/wes-2025-275
Preprint. Discussion started: 16 January 2026

7 Conclusion and outlook

In this study, we introduced a novel continuous-time wake model for simulation and optimal control of crosswind kite systems. The new model is based on a hybrid combination of infinitesimal vortex-loop and dipole elements shedded by the kites. Compared to existing vortex-based approaches, the model is capable of capturing the inherently unsteady and non-axisymmetric nature of how crosswind kite systems operate. Validation with the higher-fidelity free-vortex code DUST shows a good agreement between the two simulations. One remaining point of mismatch is the wake convection velocity. In this study, three different heuristics for selecting the convection velocity were compared, and a best candidate was selected. However, this candidate overestimates the convection velocity, resulting in a remaining $5\,\%$ overestimation of the aerodynamic forces produced in the validation simulations. The model is also very well able to capture the induced velocity field around the wing trajectory flown, suggesting that it is well-suited for optimization purposes.

As a second contribution, we proposed a formulation that allows one to efficiently incorporate thew new wake model into periodic optimal control problems. The formulation exploits the periodicity of the wake and its efficacy particularly hinges on the introduction of a moving window of influence that only considers the part of the wake within a certain region around the flying wings' trajectory. Using an accurate reference parameterization of the wake model, the original OCP cost is increased with a factor of 16. However, if we tolerate a loss of accuracy of $5\,\%$ compared to this reference, we can achieve a modest slowdown of a factor of 3 compared to the original problem (which deviates from the reference solution with $145\,\%$).

Apart from improving the model validity, future work should focus on improving the window of influence used in the OCP formulation. Ideally, this window would move continuously along with the wing and not just update as the wing passes from one interval to the next. Such an improvement would eliminate oscillations in the time-resolved induced velocity profile and result in a consistent integration accuracy for the induced velocity expression.

In this work, we applied the new model to a dual-kite system and optimized its flight trajectory, consisting of one single loop, for maximum pulling force. Future work could focus on expanding to the following applications. First, we could extend the current example to a multi-loop scenario, where the wings fly multiple (possibly differing) loops within one period. While in the current one-loop example, the wings cannot escape their own wake, in this new scenario, the wings would be able to adapt their trajectory during the subsequent loops to avoid the wake from the previous ones, thereby boosting performance. Second, future research could investigate the application to the single-wing airborne wind energy systems currently pursued by AWE industry. While the flight trajectories of these systems are characterized by longer time periods as considered in the example of this paper, therefore necessitating a larger number of discrete wake elements, the wake model could still remain numerically tractable. Because of the long time period and long convection distance, it is likely that the initial vortex-loop part of the hybrid wake can be discarded in favor of the cheaper vortex dipole model, with less wake duplicates needed. This application would then enable one to compute wake-sensitive flight trajectories, and provide an important stepping stone to realistically assess the achievable power density of these systems.

Appendix A: Induced velocity expression of a vortex-loop element with finite width

Consider a vortex loop element as visualized in Fig. 1, characterized by the state $y := (q_\mathrm{v}, \Gamma, e_\mathrm{n}, e_\mathrm{c})$, and with a finite height $\frac{\pi}{4}b$ and width Δs. The velocity induced by this element at a position q is given by applying the Biot-Savart law to all four finite vortex filaments of the vortex-loop:

$$u_\mathrm{vl}(q, y, \Delta s) := \sum_{i=1}^{4} u_{\mathrm{f},i} \, , \tag{A1}$$

with

$$u_{\mathrm{f},1} := u_{\mathrm{f,bs}}(q, p_1, e_\mathrm{b}, \frac{\pi b}{4}, \Gamma) \tag{A2}$$

$$u_{\mathrm{f},2} := u_{\mathrm{f,bs}}(q, p_2, e_\mathrm{c}, \Delta s, \Gamma) \tag{A3}$$

$$u_{\mathrm{f},3} := u_{\mathrm{f,bs}}(q, p_3, -e_\mathrm{b}, \frac{\pi b}{4}, \Gamma) \tag{A4}$$

$$u_{\mathrm{f},4} := u_{\mathrm{f,bs}}(q, p_4, -e_\mathrm{c}, \Delta s, \Gamma) \, , \tag{A5}$$

where $e_\mathrm{b} := e_\mathrm{n} \times e_\mathrm{c}$ and where the four corners (counterclockwise) are:

$$p_1 = q_v - \frac{\Delta s}{2} e_c - \frac{\pi b}{8} e_b, \tag{A6}$$

$$p_2 = q_v - \frac{\Delta s}{2} e_c + \frac{\pi b}{8} e_b, \tag{A7}$$

$$p_3 = q_v + \frac{\Delta s}{2} e_c + \frac{\pi b}{8} e_b, \tag{A8}$$

$$p_4 = q_v + \frac{\Delta s}{2} e_c - \frac{\pi b}{8} e_b \, , \tag{A9}$$

and with the Biot-Savart evaluation function

$$u_{\mathrm{f,bs}}(q, p, e, \ell, \Gamma) := -\frac{\Gamma}{4\pi \left\| r_1 \times e \right\|^2} (r_1 \times e) \left(\frac{e \cdot r_1}{\|r_1\|} - \frac{e \cdot r_2}{\|r_2\|} \right) \, , \tag{A10}$$

where $r_1 := q - p$ and $r_2 := r_1 - \ell e$, with ℓ the vortex filament length, and e its unit direction vector. The linearization $\frac{\mathrm{d}u_\mathrm{vl}}{\mathrm{d}\Delta s}$ used in Eq. 23 is finally obtained through algorithmic differentiation using `CasADi`.

Code availability. The code used to formulate and solve the optimal control problems is available as part of the `AWEbox` toolbox at https://github.com/awebox/awebox/tree/mawero. The toolchain that generates DUST input files from `AWEbox` results (including those obtained in this paper) is available under the name `AWEWA` at https://github.com/Toni2412/AWEWA. `DUST` is open source and available online at https://www.dust.polimi.it/.

Author contributions. Methodology, JDS, AM, RL, MD; formal analysis, JDS, AM; project administration, JDS, MD; resources, MD; supervision, JDS, MD; writing – original draft, JDS; writing – review and editing, AM, RL, MD; funding acquisition, JDS, MD.

eawe european academy of wind energy
Open Access WIND ENERGY SCIENCE DISCUSSIONS

Competing interests. The authors declare no competing interests.

Acknowledgements. The authors would like to thank Gianni Cassoni and the DUST developers for their support setting up the DUST simulations. The authors used ChatGPT to improve the flow and writing quality of the scientific text at some locations. The authors reviewed and edited the content as needed and take full responsibility for the content of the publication.

Financial support. This research was supported by DFG via the project 525018088 (MAWERO).

References

Akberali, A., Kheiri, M., and Bourgault, F.: Generalized aerodynamic models for crosswind kite power systems, Journal of Wind Engineering and Industrial Aerodynamics, 215, 2021.

Andersson, J. A. E., Gillis, J., Horn, G., Rawlings, J. B., and Diehl, M.: CasADi – A software framework for nonlinear optimization and optimal control, Mathematical Programming Computation, 11, 1–36, https://doi.org/10.1007/s12532-018-0139-4, 2019.

Branlard, E.: Wind Turbine Aerodynamics and Vorticity-Based Methods, Springer-Cham, 2017.

De Lellis, M., Reginatto, R., Saraiva, R., and Trofino, A.: The Betz limit applied to Airborne Wind Energy, Renewable Energy, 127, 32–40, 2018.

De Schutter, J., Leuthold, R., and Diehl, M.: Optimal Control of a Rigid-Wing Rotary Kite System for Airborne Wind Energy, in: Proceedings of the European Control Conference (ECC), 2018.

De Schutter, J., Harzer, J., and Diehl, M.: Vertical Airborne Wind Energy Farms with High Power Density per Ground Area based on Multi-Aircraft Systems, European Journal of Control, 74, 100 867, https://doi.org/https://doi.org/10.1016/j.ejcon.2023.100867, 2023a.

De Schutter, J., Leuthold, R., Bronnenmeyer, T., Malz, E., Gros, S., and Diehl, M.: AWEbox: An Optimal Control Framework for Single- and Multi-Aircraft Airborne Wind Energy Systems, Energies, 16, 1900, https://doi.org/10.3390/en16041900, 2023b.

Fagiano, L., Quack, M., Bauer, F., Carnel, L., and Oland, E.: Autonomous Airborne Wind Energy Systems: Accomplishments and Challenges, Annual Review of Control, Robotics, and Autonomous Systems, 5, 603–631, https://doi.org/10.1146/annurev-control-042820-124658, 2022.

Fritz, F.: Airborne Wind Energy, chap. Application of an Automated Kite System for Ship Propulsion and Power Generation, pp. 391–411, Springer-Verlag Berlin Heidelberg, 2013.

Gaunaa, M., Forsting, A. M., and Trevisi, F.: An engineering model for the induction of crosswind kite power systems, Journal of Physics: Conference Series, 1618, 032 010, 2020.

Gros, S. and Diehl, M.: Modeling of Airborne Wind Energy Systems in Natural Coordinates, in: Airborne Wind Energy, Springer-Verlag Berlin Heidelberg, 2013.

Gros, S. and Zanon, M.: Numerical Optimal Control with Periodicity Constraints in the Presence of Invariants, IEEE Transactions on Automatic Control, 63, 2818–2832, 2018.

Gros, S., Zanon, M., and Diehl, M.: A Relaxation Strategy for the Optimization of Airborne Wind Energy Systems, in: Proceedings of the European Control Conference (ECC), pp. 1011–1016, 2013.

Haas, T., De Schutter, J., Diehl, M., and Meyers, J.: Wake characteristics of pumping mode airborne wind energy systems, Journal of Physics: Conference Series, 2019.

Hart, C.: Kites: a Historical Survey, Paul P. Appel Publisher, 1982.

Heydarnia, O., Wauters, J., Lefebvre, T., and Crevecoeur, G.: Optimal Path Planning of Airborne Wind Energy Systems with a Flexible Tether, Journal of Guidance, Control and Dynamics, pp. 1–8, 2025.

Horn, G., Gros, S., and Diehl, M.: Numerical Trajectory Optimization for Airborne Wind Energy Systems Described by High Fidelity Aircraft Models, in: Airborne Wind Energy, Springer-Verlag Berlin Heidelberg, 2013.

HSL: A collection of Fortran codes for large scale scientific computation., http://www.hsl.rl.ac.uk, 2011.

Joshi, R., Schmehl, R., and Kruijff, M.: Power curve modelling and scaling of fixed-wing ground-generation airborne wind energy systems, Wind Energy Science, 9, 2195–2215, 2024.

Kaufman-Martin, S., Naclerio, N., May, P., and Luzzatto-Fegiz, P.: An entrainment-based model for annular wakes, with applications to airborne wind energy, Wind Energy, 25, 419–431, https://doi.org/https://doi.org/10.1002/we.2679, 2022.

Kheiri, M., Nasrabad, V. S., and Bourgault, F.: A new perspective on the aerodynamic performance and power limit of crosswind kite systems, Journal of Wind Engineering and Industrial Aerodynamics, 2019.

Kokkedee, J.: Wind farm wake flow recovery with the use of kites, Master's thesis, Delft University of Technology, 2022.

Leuthold, R., Gros, S., and Diehl, M.: Induction in Optimal Control of Multiple-Kite Airborne Wind Energy Systems, in: Proceedings of 20th IFAC World Congress, Toulouse, France, 2017.

Leuthold, R., De Schutter, J., Malz, E. C., Licitra, G., Gros, S., and Diehl, M.: Operational Regions of a Multi-Kite AWE System, in: European Control Conference (ECC), https://doi.org/10.23919/ECC.2018.8550199, 2018.

Leuthold, R., De Schutter, J., Crawford, C., Gros, S., and Diehl, M.: Rigid-Wake Lifting-Line Vortex Modeling in a Single-Kite AWE Optimal Control Problem, in: Book of Abstracts of the Airborne Wind Energy Conference 2024, 2024.

Loyd, M.: Crosswind Kite Power, Journal of Energy, 4, 106–111, 1980.

Malz, E., Verendel, V., and Gros, S.: Computing the Power Profiles for an Airborne Wind Energy System based on Large-Scale Wind Data, Renewable Energy, 2020.

Manwell, J. F., McGowan, J. G. and Rogers, A. L.: Wind Energy Explained: Theory, Design and Application, Second Edition, John Wiley & Sons, Ltd, Chichester, UK, 2009.

Noga, R., Paulig, X., Schmidt, L., Karg, B., Quack, M., and Soliman, M.: Optimization of 3-D flight trajectory of variable trim kites for airborne wind energy production, in: Proceedings of the European Control Conference (ECC), 2024.

Ploumakis, E. and Bierbooms, W.: Enhanced Kinetic Energy Entrainment in Wind Farm Wakes: Large Eddy Simulation Study of a Wind Turbine Array with Kites, pp. 165–185, Springer Singapore, Singapore, ISBN 978-981-10-1947-0, https://doi.org/10.1007/978-981-10-1947-0_8, 2018.

Trevisi, F., Castro-Fernández, I., Pasquinelli, G., Riboldi, C. E. D., and Croce, A.: Flight trajectory optimization of Fly-Gen airborne wind energy systems through a harmonic balance method, Wind Energy Science, 7, 2039–2058, 2022.

Trevisi, F., Riboldi, C., and Croce, A.: Vortex model of the aerodynamic wake of airborne wind energy systems, Wind Energy Science, 8, 999–1016, https://doi.org/10.5194/wes-8-999-2023, 2023.

Tugnoli, D., Montagnani, D., Syal, M., Droandi, G., and Zanotti, A.: Mid-fidelity approach to aerodynamic simulations of unconventional VTOL aircraft configurations, Aerospace Science and Technology, p. 106804, 2021.

Van Niekerk, T.: Enhancing Wind Farm Wake Recovery Through Kite-Induced Vertical Entrainment, Master's thesis, Delft University of Technology, 2025.

Vermillion, C., Cobb, M., Fagiano, L., Leuthold, R., Diehl, M., Smith, R. S., Wood, T. A., Rapp, S., Schmehl, R., Olinger, D., and Demetriou, M.: Electricity in the air: Insights from two decades of advanced control research and experimental flight testing of airborne wind energy systems, Annual Reviews in Control, 52, 330–357, https://doi.org/https://doi.org/10.1016/j.arcontrol.2021.03.002, 2021.

Wächter, A. and Biegler, L. T.: On the implementation of an interior-point filter line-search algorithm for large-scale nonlinear programming, Mathematical Programming, 106, 25–57, 2006.

Zanon, M., Gros, S., Andersson, J., and Diehl, M.: Airborne Wind Energy Based on Dual Airfoils, IEEE Transactions on Control Systems Technology, 21, 1215–1222, https://doi.org/10.1109/TCST.2013.2257781, 2013.

Zanon, M., Gros, S., Meyers, J., and Diehl, M.: Airborne Wind Energy: Airfoil-Airmass Interaction, in: Proceedings of the IFAC World Congress, pp. 5814–5819, 2014.